Lattice-Boltzmann modeling of lifted hydrogen jet flames: a new model for hazardous ignition prediction

Said Taileb[1], Alejandro Millán-Merino, Song Zhao, Pierre Boivin[2]

[a] *Aix Marseille Univ, CNRS, Centrale Marseille, M2P2, Marseille, France*

Abstract

This numerical study deals with the hazardous ignition of a jet flame in a vitiated co-flow. A novel formulation, based on a passive scalar variable, will be presented to predict hydrogen auto-ignition events. The model, derived from the theoretical analysis of the Jacobian, correctly describes the appearance and absence of auto-ignition in complex configurations based on initial thermodynamic and mixture conditions. No chemical reaction and species equations are required to perform the simulations. Results of Lattice Boltzmann Methods (LBM) simulations of a 3D H_2/N_2 Cabra flame will be presented using a detailed H_2-Air mechanism. Validation against experimental and numerical results will be provided for the lift-off (distance to auto-ignition). The passive scalar predictions are successfully compared with the reactive simulations. The results show a potential extension of this model to an extensive spectrum of hydrogen safety and large-scale turbulent combustion applications.

Keywords: Lattice-Boltzmann methods; auto-ignition; hydrogen; turbulent combustion

[1]Corresponding authors: `said.taileb@univ-amu.fr`

[2]`pierre.boivin@univ-amu.fr`

1. Introduction

The looming environmental crisis calls for new designs and technologies, especially in the frowned-upon field of combustion. Significant research efforts are being invested worldwide in the study of hydrogen combustion applications, which are up-to-date mostly limited to space applications: the large flammability limits [1] of H_2 bring exceptional challenges in democratizing the H_2 usage beyond rocketry.

In particular, the risk of explosion due to H_2 leaks in hot regions is particularly hard to predict: when designing a new technology (e.g. a hydrogen aircraft), the relevant question is not whether the system will leak, but how much it will leak. Luckily, the three hydrogen explosion limits reported by Lewis and von Elbe [2] are well understood now [1, 3], and accurate analytical descriptions of hydrogen ignition are available in most regimes [4–9].

In particular, we will focus on turbulent lifted hydrogen jet flames, a configuration reminiscent of hydrogen leaks igniting in a hot environment. The hydrogen lifted flame experimentally investigated by Cabra et al. [10] is an excellent case to investigate such problem. The ignition distance is known to be highly sensitive to the ambient conditions: a 1% difference in ambient temperature may lead to doubling (or halving) the lift-off. In conditions close to crossover, a small temperature decrease can mean complete extinction of the flame (e.g. no ignition). For this reason, a large number of simulations of this configuration is reported in the literature [11–18]. Later, several experiments [19, 20] provided a parametric study for a wide range of co-flow temperatures and injection velocities. These authors have identified

various regimes noted as: no ignition, random spots, flashback, and lifted flame regimes. For the random spot regime which is in a relatively narrow temperature range (5K), independent kernels appear and are advected before they disappear, a regime identified as a transition to MILD combustion [21].

This study's objective is twofold. First, we will show that the recent hybrid Lattice-Boltzmann model [22–25] presented by our group for reactive flows is able to accurately model such a sensitive turbulent lifted flame. This is, to the authors' knowledge, the first attempt of Lattice-Boltzmann simulation of a 3D turbulent reactive jet. A brief introduction on Lattice-Boltzmann modeling of reacting flows is provided in Sec. 2.2

Second, we will present a single passive scalar model to predict the risk of hazardous ignition, based on the aforementioned analytical descriptions of H_2 ignition. This model builds upon cold flow simulations (e.g. without combustion source term) only involving the main reactants to reproduce the mixing. The model is of high interest in the community: (i) it is much easier to simulate cold flow than reactive flow; (ii) since the scalar is passive, simulations are much less sensitive to the chemical characteristic time constrain, known to be especially stark for hydrogen; and (iii), simulations are much cheaper: the chemical time constraint less stiff than for detailed chemistry, and there is no further need to transport all 9 species of the detailed mechanism.

The model will be shown to accurately predict lift-off in configurations where ignition occurs, as well as the absence of ignition when the ambient temperature is slightly decreased.

2. Numerical method

2.1. Governing equations

In the present work, the motion, transport and chemical reactions of the species present in the gas mixture are modeled using the reactive Navier-Stokes equations

$$\frac{\partial \rho}{\partial t} + \frac{\partial \rho u_\beta}{\partial x_\beta} = 0 \tag{1}$$

$$\frac{\partial \rho u_\alpha}{\partial t} + \frac{\partial \rho u_\alpha u_\beta + p\delta_{\alpha\beta}}{\partial x_\beta} = \frac{\partial \tau_{\alpha\beta}}{\partial x_\beta} \tag{2}$$

$$\frac{\partial \rho E}{\partial t} + \frac{\partial \rho u_\beta (E + p/\rho)}{\partial x_\beta} = \frac{\partial \tau_{\alpha\beta} u_\alpha}{\partial x_\beta} - \frac{\partial q_\beta}{\partial x_\beta} \tag{3}$$

$$\frac{\partial \rho Y_k}{\partial t} + \frac{\partial \rho u_\beta Y_k}{\partial x_\beta} = \frac{\partial \rho V_{k,\beta} Y_k}{\partial x_\beta} + \dot{\omega}_k \tag{4}$$

Here u_α is the α^{th} component of the fluid velocity, ρ is the density of the mixture, E is the total energy, and Y_k is the mass fraction of species k. The species diffusion velocity $V_{k,\alpha}$ is computed through

$$V_{k,\alpha} = -\frac{\mathcal{D}_k}{X_k}\frac{\partial X_k}{\partial x_\alpha} + V_\alpha^c \tag{5}$$

via a constant Lewis number for the diffusion coefficient $\mathcal{D}_k = \lambda/(\rho C_p \mathrm{Le}_k)$ of the k species and the conservative flux correction [26]

$$V_\alpha^c = \sum_{k=1}^{N} Y_k \frac{\mathcal{D}_k}{X_k}\frac{\partial X_k}{\partial x_\alpha}, \tag{6}$$

with X_k the mole fraction of the k species. The mass production or consumption rate $\dot{\omega}_k$ is calculated using the 12-step reduced mechanism for hydrogen combustion derived by Boivin et al. [7]. In the energy equation (3), the thermal heat flux term q_α is obtained using the generalized Fourier's Law

$$q_\alpha = -\lambda\frac{\partial T}{\partial x_\alpha} + \rho\sum_{k=1}^{N} h_k Y_k V_{k,\alpha} \tag{7}$$

where h_k is the enthalpy of the k species and $\lambda = \mu C_p/\mathrm{Pr}$ is the thermal conductivity of the mixture defined as function of the mixture viscosity μ, its heat capacity C_p, and a constant Prandtl number Pr. In the momentum equation (2) the viscous stress tensor $\tau_{\alpha\beta}$ is defined as

$$\tau_{\alpha\beta} = (\mu + \mu_t)\left(\frac{\partial u_\alpha}{\partial x_\beta} + \frac{\partial u_\beta}{\partial x_\alpha} - \frac{2}{3}\delta_{\alpha\beta}\frac{\partial u_\gamma}{\partial x_\gamma}\right) \tag{8}$$

where μ_t is the turbulent viscosity defined hereafter, $\delta_{\alpha\beta}$ is the Kronecker symbol and the dynamic viscosity of the mixture, that is defined by $\mu = \mu_0(T/T_0)^{0.7}$ with the sub-index 0 representing the reference value at atmospheric conditions. The previous set of equations is closed after specifying the ideal gas of equation,

$$\frac{p}{\rho} = \frac{\mathcal{R}}{W}T \tag{9}$$

where p, T and $\mathcal{R}$ are the pressure, temperature and the ideal gas constant, respectively, and the constitutive relations

$$\frac{1}{W} = \sum_{k=1}^{N}\frac{Y_k}{W_k}, \quad C_p = \sum_{k=1}^{N} C_{p,k}Y_k, \quad h = \sum_{k=1}^{N} h_k Y_k \tag{10}$$

in terms of the heat capacity, $C_{p,k}$, enthalpy h_k, and molecular weight W_k of the k species. The temperature dependence thermodynamic properties of the individual species are computed using the NASA polynomials [27].

To account for the smallest flow structure and maintain a reasonable grid size, the Vreman's subgrid model is used [28]. This model contains a correction in the dynamic viscosity of the momentum equation such that $\mu = \mu + \mu_t$, where μ_t is the turbulent Vreman viscosity [28]. Validation against turbulent shear flows, transitional flows and near wall region have shown a very interesting self adaptation without using a dynamics procedure or clipping. The

computational cost is drastically reduced thanks to the absence of eigenvalue computations [29, 30]. Hereafter, no turbulent combustion model is used, following other similar studies [31].

Diffusion species coefficients are defined through constant Schmidt numbers for each chemical species, associated with a Lewis number for each species. A constant Prandtl number of Pr = 0.75 is combined with a constant thermal conductivity. For the turbulent modeling, we have retained turbulent Prandtl and Schmidt numbers of 0.6.

2.2. Compressible hybrid Lattice-Boltzmann model

Recent progress in numerical combustion allows more affordable studies of combustion [26]. Lattice Boltzmann Methods (LBM) are experiencing an important increase in several applications such as external aerodynamics and aero-acoustics for several industrial applications [32–34]. Compared to classical numerical methods, it requires less communication and memory transfer between processors (CPU's) resulting in highly scalable code [25]. Indeed, the LBM methods are based on a local nonlinear collision step and non-local linear propagation step [35, 36]. Moreover, a second-order accuracy in space and time can be obtained with a very small dissipation of pressure waves comparable to high order methods. However, their application to combustion requires taking into account energy conservation and mass fraction of chemical species equations. Hence several strategies can be found in literature such as multiple relation time [37], central cascade moment [38–41], Entropic [42] and Cumulants [43–45] of Lattice Boltzmann equation. Among these efforts, our group have contributed recently through hybrid recursive regularized LBM [46] based on density (HRR-ρ) [24, 47] to tackle combustion

using LB for mass and momentum and finite differences (FD) to energy and species conservation.

Because of the rather low number of discrete velocities (19), the energy equation cannot be recovered directly from the LB quantities and is therefore solved in parallel by an especially designed numerical scheme. For simplicity, species are resolved using the same strategy. Indeed, the coupling is paramount for the solver stability. This coupling was thoroughly presented and studied in Farag's recent works [22, 24, 48].

Note that the model was validated on a wide variety of test cases, from simple Kovasznay mode propagations [22, 24] and canonical 1D and 2D flames [23, 49]; to thermo-diffusive [50] and thermo-acoustic instabilities [51]. The competitivity of the proposed algorithm was also demonstrated on both a DNS benchmark [25] and the simulation of turbulent premixed combustion in a 3D burner [52].

2.2.1. LB solver for Mass and momentum equation

The classical Navier-Stokes (NS) equations are reconstructed based on the Boltzmann equation (BE) model for the kinetic theory of gas. Neglecting external forces, the BE equation can be defined through a particle velocity distribution function (VDF) $f(\boldsymbol{x}, \boldsymbol{\xi}, t)$ that reads

$$\frac{\partial f}{\partial t} + \boldsymbol{\xi} \frac{\partial f}{\partial \boldsymbol{x}} = -\frac{1}{\tau}(f - f^{eq}) \tag{11}$$

where $\boldsymbol{\xi}$ being particles velocity at location $\boldsymbol{x}$ and time t. The left-hand side of equation (11) governs the free streaming particles while the right-hand side controls their collisions. τ is the relaxation time associated with the dynamic viscosity of the fluid known as the Bhatnagar-Gross-Krook (BGK)

collision operator. f^{eq} is the Maxwellian equilibrium distribution function at which f relax through collisions. This function is associated with the local thermodynamic state

$$f^{eq} = \frac{\rho}{(2\pi\mathcal{R}T)^{3/2}} e^{-(||\boldsymbol{\xi}-\boldsymbol{u}||^2)/\mathcal{R}T} \tag{12}$$

The conservation equations of mass and momentum can be expressed as follows. The macroscopic variables are recovered from VDF as follows

$$\rho = \int f d\boldsymbol{\xi} \tag{13}$$

$$\rho\boldsymbol{u} = \int f\boldsymbol{\xi} d\xi \tag{14}$$

Chapman-Enskog [23, 53] or Taylor expansion [48] show time and space second-order equivalence with the governing equations (1-2). The LB equation is solved using a hybrid regularized collision model [54]. The streaming and the collision operations are expressed as follows

$$\textbf{Streaming :} \quad f_i(t+\delta t, \boldsymbol{x}) = f_i^{\text{col}}(t, \boldsymbol{x} - \boldsymbol{c}_i\delta t) \tag{15}$$

$$\textbf{Collision :} \quad f_i^{\text{col}} = f_i^{\text{eq}} + \left(1 - \frac{\delta t}{\overline{\tau}}\right) f_i^{\text{neq}} + \frac{\delta t}{2} F_i^{\text{E}} \tag{16}$$

where δt is the time step, $\boldsymbol{c}_i$ presents the i^{th} velocity of the lattice. Distribution functions for equilibrium and non-equilibrium presented as f_i^{eq}, f_i^{neq} and F_i^{E} are equilibrium part, the non-equilibrium part and the forcing terms for the viscous tensor. These quantities are evaluated from their projection onto the D3Q19 rotational symmetry basis of Gauss-Hermite polynomials up to third order as in Jacob et al. [54]. Additional higher-order polynomials

are chosen by "moment matching" to be as close as possible to the D3Q27 lattice in order to recover some flow iso-tropic properties [55, 56]. Further details can be found in the supplemental material.

2.2.2. Ad-hoc finite difference solver for energy and species equations

Transport equations for total energy ((3)) and mass fractions ((4)) are transported using the Finite Difference (FD) method. Conservative numerical schemes specially designed for hybrid LBM-FD methods are applied for the Euler part of the flux [57]. The total energy flux is calculated using the LBM population, i.e.

$$\nabla^{\mathrm{U}} \cdot (\rho \boldsymbol{u} H) \equiv \sum_i \left[f_i^{\mathrm{col}}(t, \boldsymbol{x}) H(t, \boldsymbol{x}) - f_i^{\mathrm{col}}(t, \boldsymbol{x} - \boldsymbol{c_i}\delta t) H(t, \boldsymbol{x} - \boldsymbol{c_i}\delta t) \right] \quad (17)$$

with $H \equiv E + p/\rho$ the total enthalpy. The species transport terms are evaluated in a similar manner. In order to reduce the numerical dissipation, a combination of the Osmanlic upwind scheme and the skew-symmetry centre scheme is utilized, i.e.

$$\nabla^{\mathrm{H}} \cdot (\rho \boldsymbol{u} Y_k) \equiv \alpha^{\mathrm{UP}} \nabla^{\mathrm{OS}} \cdot (\rho \boldsymbol{u} Y_k) + \left(1 - \alpha^{\mathrm{UP}}\right) \nabla^{\mathrm{C}} \cdot (\rho \boldsymbol{u} Y_k) \quad (18)$$

Readers are referred to [57, 58] for detailed expression of the corresponding numerical operators. The diffusive and chemical source terms are also evaluated using the classical FD method, which is identical to our previous works [23, 25, 52]. Finally, the temporal integration is considered with the explicit first-order Euler scheme. The numerical simulations in the current study were performed using the massively parallel software ProLB [54, 59–61].

3. Simulation of a turbulent lifted hydrogen flame

3.1. Computational domain, boundary and initial conditions

A sketch of the classical lifted turbulent H_2 jet flame vitiated in a hot coflow, as was studied by Cabra et al. in [10], is shown in Fig. 1. Hydrogen

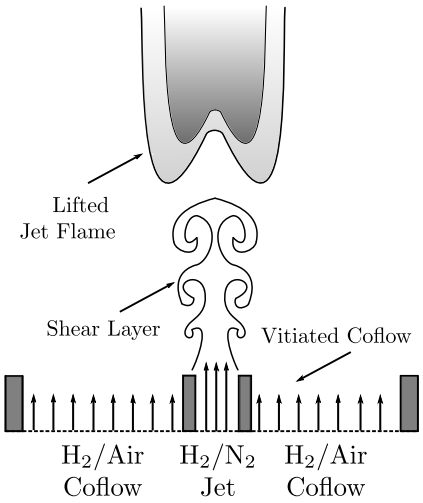

Figure 1: Jet configuration experimental setup and flame structure from Cabra et al. [10].

is injected through a central jet, surrounded by a hot vitiated co-flow of H_2-air combustion products. The co-flow temperature is high enough to ensure the auto-ignition of the gas mixture, creating a lifted flame. The computational domain used in our study is summarized in Fig. 2. The characteristic outflow boundary conditions were specified at the far-field, by giving the ambient pressure to $p_0 = 101325$ Pa. The inlet conditions for the jet and the co-flow were set by imposing an inflow boundary condition with their velocity, temperature and species mass fractions values fixed. The main parameters are summarised in Tab. 1. The splitter between the two in-flow streams is treated as an iso-thermal slip wall.

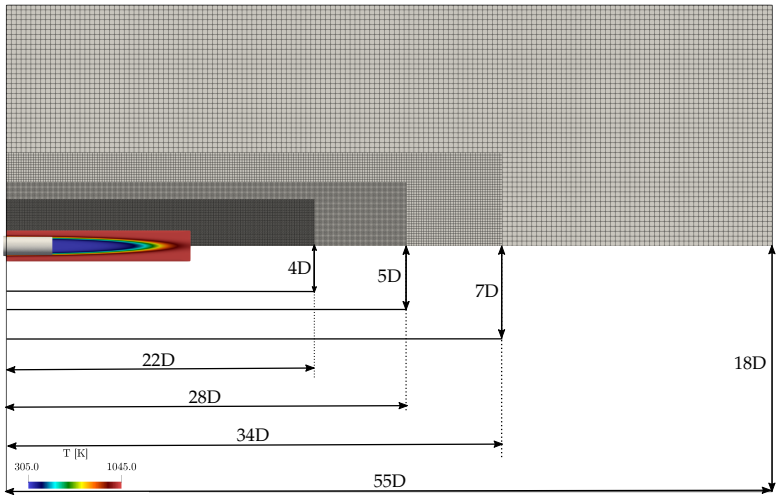

Figure 2: Initial conditions and grid refinement strategy.

The computational domain size is $55 \times 36 \times 36D$, and consists of four grid levels, with the finest level covering $22 \times 8 \times 8D$, corresponding to the full region of interest: the mixing, induction and reaction zone. The resulting mesh consists of 17 million grid points, with the finest region corresponding to 20 points in the jet diameter ($\delta_x = 2 \times 10^{-4}$m). At each grid transition, spatial and temporal discretizations are doubled. The time-step on the finest grid is $\delta_t = 1 \times 10^{-7}$ s, corresponding to a maximum CFL value of 0.42 for the reactive simulations.

The initial conditions, illustrated in Fig. 2, are defined through introduction of

$$\Phi = \frac{1}{2}\left[1 - \tanh \frac{|\boldsymbol{x} - \boldsymbol{x_0}| - R_0}{\boldsymbol{\delta}}\right]$$

were Φ is an ad-hoc function defined such as $\Phi = 1$ close to the injector and $\Phi = 0$ elsewhere. R_0 is the jet radius while δ is the width of the shear layer, specified as $(4\Delta x,\ 1,\ 1)$ and $\boldsymbol{x}$ is the vector of spatial coordinates

such that $\boldsymbol{x_0} = (x_0,\ y_0,\ z_0)$. Hence the inlet injection conditions are $\mathcal{F}_{in} = \mathcal{F}_j\Phi + \mathcal{F}_c(1-\Phi)$, where $\mathcal{F}_j$ and $\mathcal{F}_c$ respectively correspond to the jet and coflow conditions, listed in Tab. 1.

	Central jet	Coflowing jet
D (mm)	4.57	210
T (K)	305	1045
U (m/s)	107	3.5
Re	23 600	18 600
$X_{\mathrm{H_2}}$	0.2537	0.0
$X_{\mathrm{O_2}}$	0.0	0.0989
$X_{\mathrm{N_2}}$	0.7427	0.7534
$X_{\mathrm{H_2O}}$	0.0	0.1474

Table 1: Initial conditions for the jet flame [10].

3.2. Qualitative description

Figure 3 shows the instantaneous structure of the flow with the iso-surfaces of the Q criterion at $t = 7.698$(ms) corresponding to 180 characteristic times ($t_c = D/U_{\mathrm{jet}}$). The flow seems to destabilize as the hydrogen and air come into contact at the tube outlet. Vortex structures are thus created and promote the mixing of the chemical species. Auto-ignition occurs where temperature increases at a distance from the inlet called the flame lift-off. This predicted lift-off of $\approx 10D$ is reasonable and coincides with the experimental observations [10].

In order to measure more accurately the lift-off distance two-dimensional cross-section of the flow fields observed in Fig. 3 are presented in Fig. 4, in the region between the jet inlet (identified by the white dots at coordinate $[z/D = 0, r/D = \pm 0.5]$) and $22D$. Temperature is presented at the top

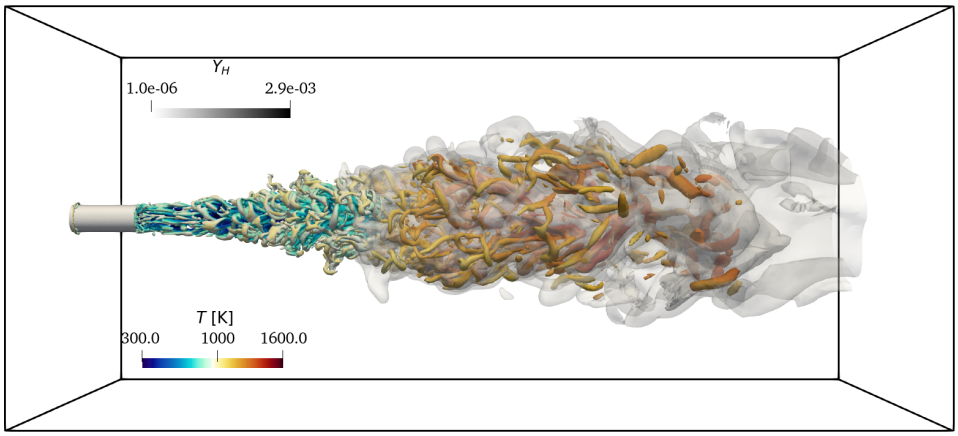

Figure 3: Instantaneous iso-surface of Q criterion, colored by temperature. Iso-contour of H radical mass fraction denoting the presence of auto-ignition (light gray).

while the mass fraction of the radical Y_{H} are presented at the bottom. The Figure confirms that auto-ignition occurs at a distance corresponding to 10D. Indeed, the temperature undergoes a significant increase from this distance indicating that the turbulent model seems to predict the right spreading rate of the round jet. In the same way, the mass fraction of the radical H increases significantly at this distance reaching its maximum value. It is then consumed in the reaction zone.

3.3. Quantitative comparison with experiments

Flow statistics using Reynolds averages were computed over 200 characteristic times, starting once the flame is well established. The mean fields are

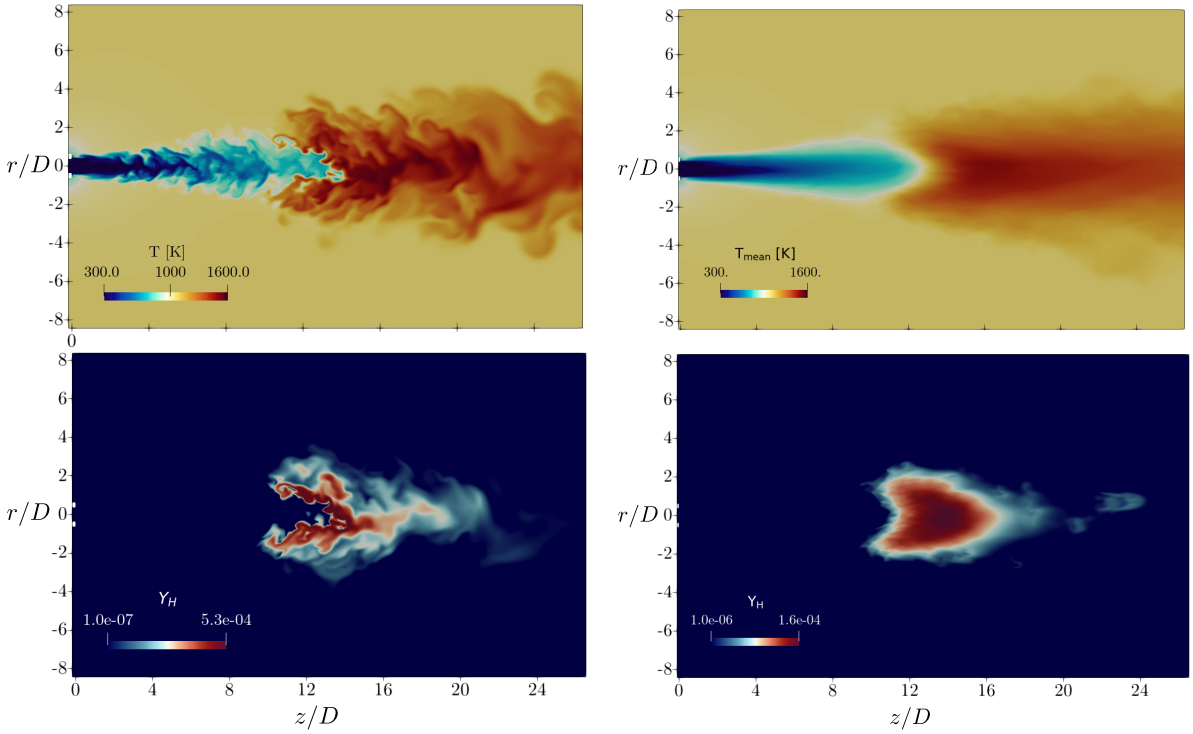

Figure 4: Two dimensional cross-section of instantaneous (left) and mean (right) flow field. Temperature displayed at the top and Y_{H} at the bottom.

presented in the right plots of Fig. 4. As with instantaneous fields, the rapid temperature increase attests the presence of auto-ignition and heat release. The mass fraction of H radicals increases rapidly in the same area showing a reactive front structure of W-shape, consistent with the triple-flame structure described in the literature.

Mean temperature and mixture fraction profiles are plotted along the centerline $r/D = 0$ and compared with experimental measurements from Cabra et al [10]. The average mixture is computed using the following expression:

$$f = \frac{(Y^j_{\mathrm{H_2}} - Y^{co}_{\mathrm{H_2}})/2W_{\mathrm{H_2}} - (Y^j_{\mathrm{O_2}} - Y^{co}_{\mathrm{O_2}})/W_{\mathrm{O_2}}}{\left[(Y^j_{\mathrm{H_2}} - Y^{co}_{\mathrm{H_2}})/2W_{\mathrm{H_2}} - (Y^j_{\mathrm{O_2}} - Y^{co}_{\mathrm{O_2}})/W_{\mathrm{O_2}}\right]_{\mathrm{inlet}}} \tag{19}$$

were inlet, j and co denote species mass fractions at the inlet, jet and co-flow, respectively. Additional numerical results extracted from the literature are also gathered in Fig. 5 and compared to the present simulation. These models combine different strategies namely probability density function (pdf) and eddy dissipation concept (EDC) for chemistry with $k - \epsilon$ and LRR (Launer, Reese, and Rodi) for turbulence [62–68]. The temperature profiles recently obtained by Wang et al. [69] using a normalised residence time transport equation are also reported.

The present simulation shows a satisfactory agreement for mixture fraction values, falling well within the prediction range of the other models. A faster consumption of fresh gas from $z/D = 10$ is observed in comparison with the experiments reaching a maximum deviation around $z/D = 15$. Further in the flame, this deviation becomes smaller to reach reasonable values in the burnt gases. The most predictive cases of the experimental at this stage are the LBM and the EDC model.

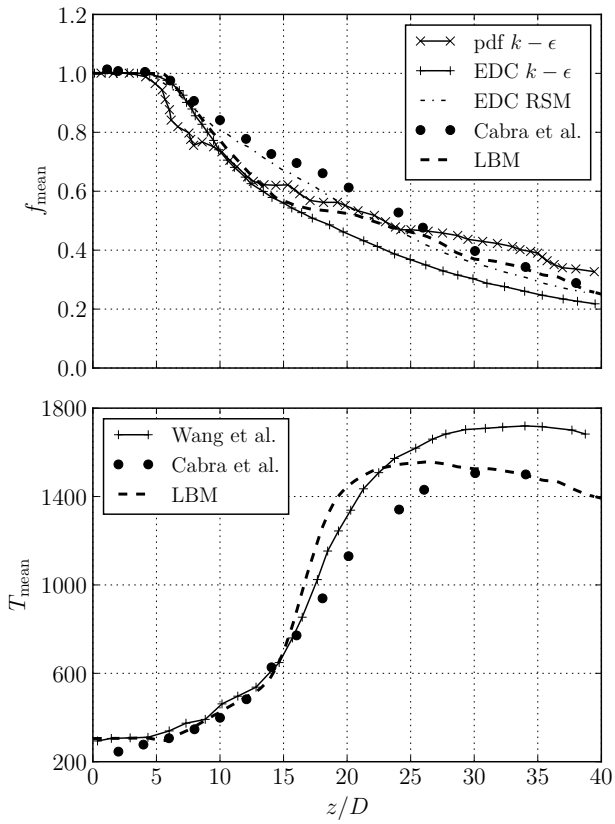

Figure 5: Mean temperature and mixture fraction for axial position. Comparison with experimental measurements by Cabra et al.[10].

The temperature profiles presented in Fig. 5 also show an excellent prediction of the experimental temperature in the induction zone (up to $z/D = 15$). The deviation obtained further is explained by the lack of a subgrid turbulent combustion model for the chemical source term, which leads to overestimating the reaction rate. This has a limited impact on the present study, however, since we will focus only on the induction region.

Finally, mean and root mean square (RMS) radial profiles are obtained by averaging along the azimuthal direction. Temperature and H_2 mass fraction are presented in Fig. 6. Different axial positions $z/D = 8,\ 11,\ 26$ are plotted before auto-ignition, reaction zone and burnt gases, respectively. Mean quantities seem to be well predicted before ignition and in the burnt gases. However, an over-prediction of temperature and an under-prediction in H_2 mass fraction can be observed at $z/D = 11$. Consistently with the earlier comment on the overestimation of heat release due to the lack of turbulent closure for the source term, one observes a faster decay of H_2 mass fractions and a higher energy release. However, (pdf) model used by Jones et al. [70] seems to provide similar results.

4. A predictive model for auto-ignition

It is well understood that the ignition process can be well represented by chained reactions building up a radical pool, which eventually will trigger heat-releasing reactions. Typically, the evolution of this radical pool has an exponential character that arises from the fact that the reaction rate is proportional to its concentration. An important change of temperature is observed in the gas mixture when the radical pool concentration reaches a certain amount. Then, the heat release exponentially accelerates the radical

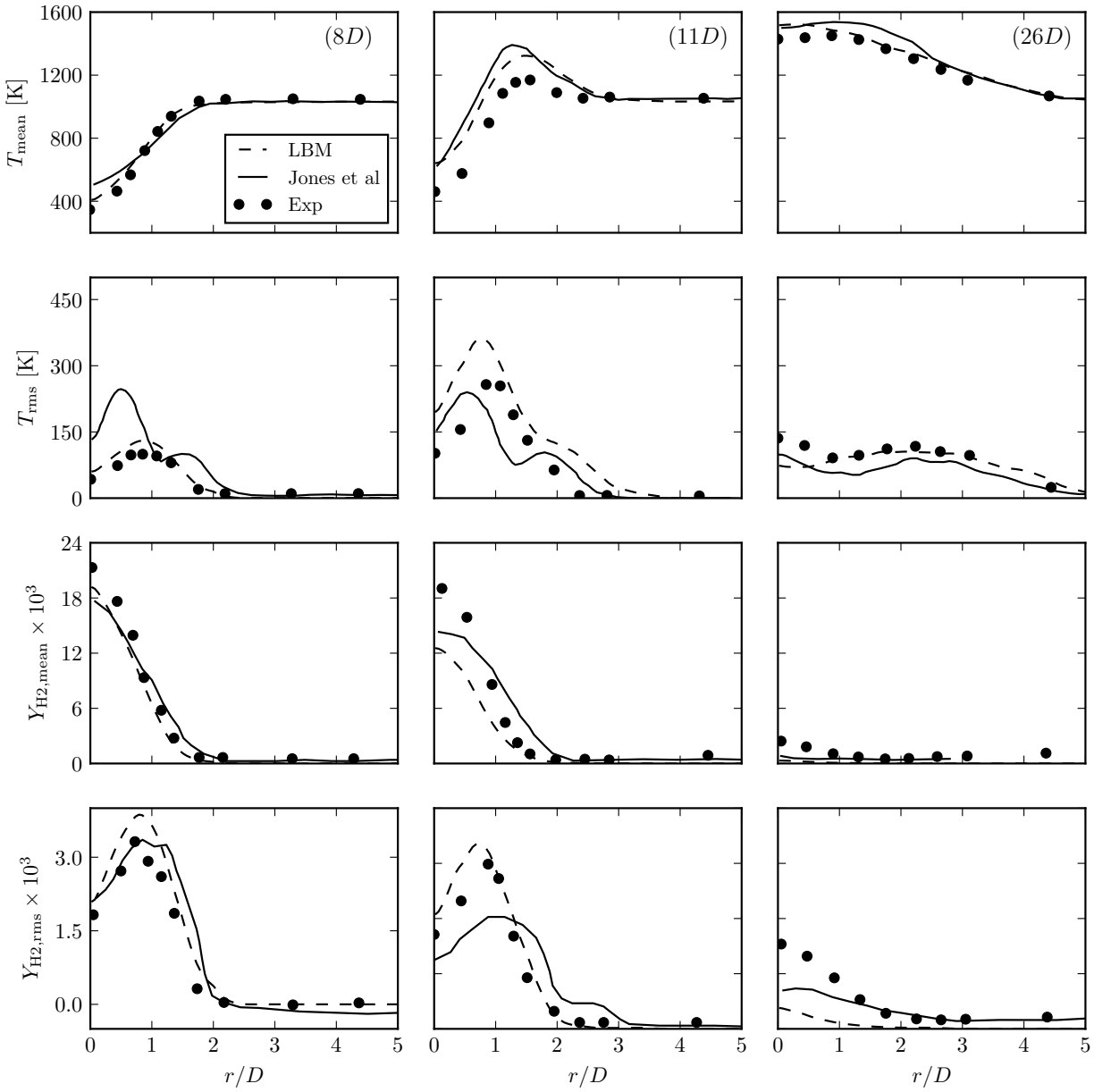

Figure 6: Mean and RMS of temperature, H_2 mass fractions for different radial positions $r/D = 8$, 11, 26. Comparison with experimental measurements conducted by Cabra et al.[10] and LES from Jones et al.[70].

pool productions yielding to a thermal-chain process known as auto-ignition ignition phenomena.

In the first approximation, if the time required for the thermal-chain integration is neglected (time between the first appreciable temperature increase $\sim$ 10K and the maximum heat release) the ignition procedures could be modelled by the time evolution of the radical pool (evaluated at the initial temperature) and thus the ignition delay time is defined as the time needed to reach a certain amount of radical pool.

In the present work, we will introduce a passive scalar, η, that play the role of the radical pool mass fraction, and it will trace and determine the ignition conditions.

4.1. Formulation

As was done for the species conservation equation (4), a transport-diffusion-reaction equation will be employed to describe the passive scalar temporal evolution as

$$\frac{\partial \rho \eta}{\partial t} + \frac{\partial \rho u_\alpha \eta}{\partial x_\alpha} = \frac{\partial}{\partial x_\alpha}\left(\frac{1}{Le_\eta}\frac{\lambda}{C_p}\frac{\partial \eta}{\partial x_\alpha}\right) + \dot{\omega}_\eta \ . \tag{20}$$

The mass production rate term, $\dot{\omega}_\eta$, is computed from the theoretical work of P. Boivin et al. [9]. Using a reduced version of the original 12-steps mechanism [7], the isothermal reaction rate of the radical pool, η, takes the form of

$$\dot{\omega}_\eta = \rho(\lambda\eta + \epsilon) \tag{21}$$

where λ is the linearized chain-branching rate and ϵ is its initiation rate. Because of the exponential growth of the radical pool, in this context, η plays the role of the dominant radical in the mixture which controls the autoignition process. In the reference mechanism, η corresponds to the monoatomic

hydrogen, H. A detailed procedure for the derivation of this source term is given in the Supplemental Material. The scalar is passive in the sense that it does not enter in the mass or energy balance and only plays the role of a tracer variable. The thermo-diffusive properties of the scalar are those of the radical H with a turbulence model based on turbulent Prandtl and Schmidt numbers of 0.6 similar to the conservation equations.

Note that, for an easy implementation, all required routines for the passive scalar formulation are made available at pierre-boivin.cnrs.fr.

4.2. Validation

Extensive computations of different H_2-Air combustion configurations were performed to test the accuracy of the passive scalar. Constant volume reactors and a one-dimensional mixing layer were used to validate the model based on the passive scalar formulation before using it on the turbulent jet configuration.

4.2.1. Perfectly-mixed homogeneous reactor

We start the validation procedure using the computations of a homogeneous reactor at constant volume to measure the ignition delay time. These computations are also used to estimate the auto-ignition conditions in the passive scalar formulation. The temporal evolution of a stoichiometric mixture of H_2-air at an initial temperature of $T_o = 1045$ K and atmospheric pressure is shown in Fig. 7. Identifying H-radical as the ignition precursor in hydrogen mixtures [71], the Y_{H} follows an exponential evolution until the temperature increase becomes appreciable. At that time, where the thermal-chain reactions become important, the reactants, as well as the temperature, suddenly change to reach their steady values and the H-radical is consumed.

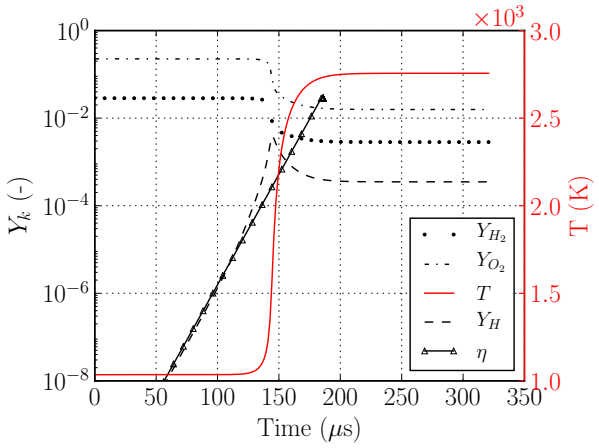

Figure 7: Ignition of stoichiometric hydrogen air mixture at $T_0 = 1045$ [K] with $p_0 = 101.35$ [kPa]. The ordinate on the right shows the temperature while the one on the left shows the mass fraction of the chemical species and the passive scalar.

In the case of the passive scalar formulation, η follows the exponential description of Y_{H}, corresponding with the exact solution in the early stages. During the ignition process, as the passive scalar formulation considers the isothermal approximation, the discrepancy between Y_{H} and η becomes appreciable. However, this difference during the ignition process only emphasizes the fact that a different definition for the ignition delay time is needed for η. Boivin et al. reported in [71] that the induction time can be estimated as the time required for the ignition precursor radical to become of the order of the initial value of the limiting reactant, $\eta(t_{\mathrm{ind}}) = \min(Y^0_{\mathrm{H_2}}, Y^0_{\mathrm{O_2}}/2)$. Since computing at each point the initial state that led to the local mixture can be tricky, and lowered the threshold based on Fig. 7 as

$$\eta(t_{\mathrm{ind}}) = \min(Y^0_{\mathrm{H_2}}, Y^0_{\mathrm{O_2}}/2)/1000 \tag{22}$$

Figure 8 presents a comparison between ignition times obtained via inte-

gration of the 12 step mechanism, and times obtained through integration of (21) until the condition (22) is fulfilled. An excellent agreement is obtained for temperatures well above crossover, with increasing departures for lower temperatures. This is expected, as the current formulation is only valid above crossover [9].

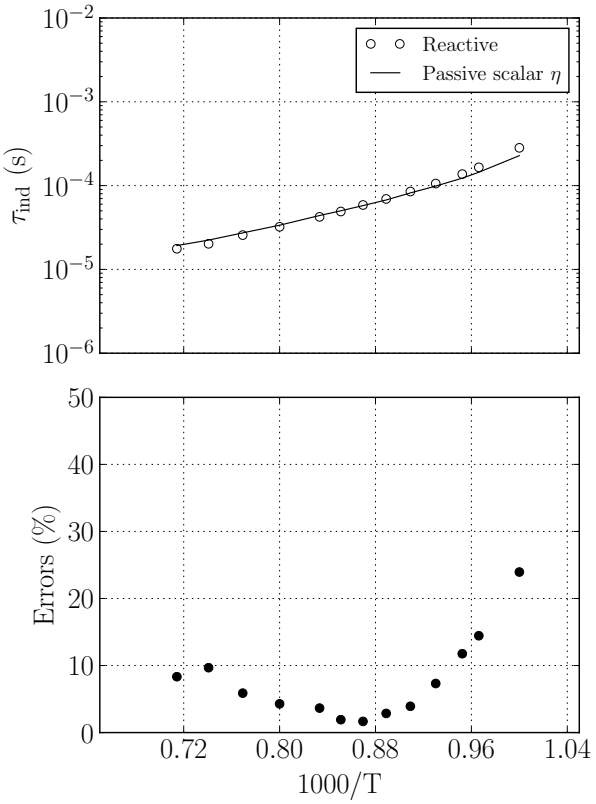

Figure 8: Top : constant volume of ignition time as function of the inverse of temperature. Initial conditions are computed at atmospheric pressure $P_0 = 1.01325 \times 10^5$ (Pa) and stoichiometric $H_2 - O_2$.

4.2.2. Triple-flame

A temporal mixing layer has been constructed by placing in contact two domains filled, on both sides, by hydrogen and air respectively. The flow

is considered to rest at atmospheric pressure and a high initial temperature $T_0 = 1045$ (K). As time passes through, the reactant are mixing and give birth to an auto-ignition in the most reactive zone. Once the ignition occurs, two premixed flame fronts, composed of lean and rich stoichiometries, propagate outward and eventually evolve into a diffusion flame. This configuration corresponds with the so-called triple-flame which can be often encountered in fuel jets applications (JHC).

In opposite with the classical homogeneous reactor, the mixing layer configuration is a stinker test case where the ignition occurs at varying local stoichiometry and the diffusion properties play an essential role in the problem. The resulting triple-flame structure can be observed in figure 9(a) with the heat release contours and the isothermal surfaces. Figure 9(b) represents Y_{H} isocontours, which are aligned with the heat release contours. Results obtained with the passive scalar model are shown in figure 9(c). Comparing Y_{H} with η it can be extracted that both follow a similar evolution in time in the early stages, where no flame is present. Later, the passive scalar continues evolving without any perturbation, in contrast to the hydrogen radical, which is consumed in the flame front and produced in excess in the fuel side because of the temperature increase.

The passive scalar model produced an underestimation of the ignition delay time about of 14% (measured by Eq. ((22)) evaluated locally) compared with the result obtained with the reference mechanism (defined as the maximum heat-release point). Looking at the location of the most reactive case, the detailed computations estimates the ignition source for an equivalence ratio of $\phi = 1.07$ while the proposed model predicts its ignition for a

lean case of $\phi = 0.22$. This discrepancy comes from two sources, firstly the ignition detection definition: although the maximum value of η is located for a richer mixture $\phi = 0.77$, the first value that reaches the condition (22) is located at a lower equivalence ratio. Secondly, the passive scalar model does not take into account the heat-release reactions that it activates, this effect will accelerate the chemistry in the stoichiometric condition, which will displace the maximum value of η to a richer equivalence ratio.

We can conclude that η model can accurately predict the presence of ignition conditions, inside the admissible chemistry uncertainties.

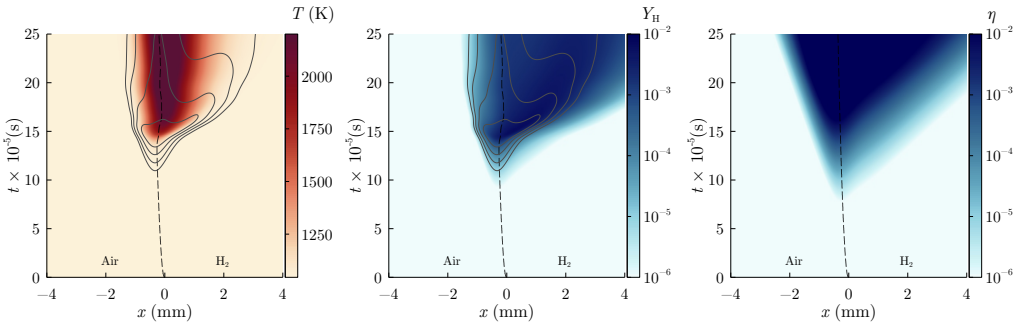

Figure 9: One-dimensional mixing layer of H_2/Air with initial temperature 1045 (K) and at atmospheric pressure $P_0 = 1.01325 \times 10^5$ (Pa). The size of the domain is $x = 30$ (mm). (a) and (b) exhibit the evolution of the temperature as well as the H radical with iso-contour of heat release rate while (c) displays the evolution of the passive scalar.

5. Auto-ignition detection applied to Cabra flame: Comparison and discussion

The non-reactive simulation presented in Fig. 10 shows the evolution of the passive scalar. Iso-surface of the Q criterion shows that the flow structure is similar to the reactive simulation where the flow becomes turbulent at the inlet. The temperature change is less noticeable and only due to the

mixing between hot co-flow and fresh hydrogen. Contours of the passive scalar are presented around the auto-ignition criteria η_{ignit} with a transparent grey color. The passive scalar follows the same behavior as the H radical giving a similar rate of increase in the reactive case.

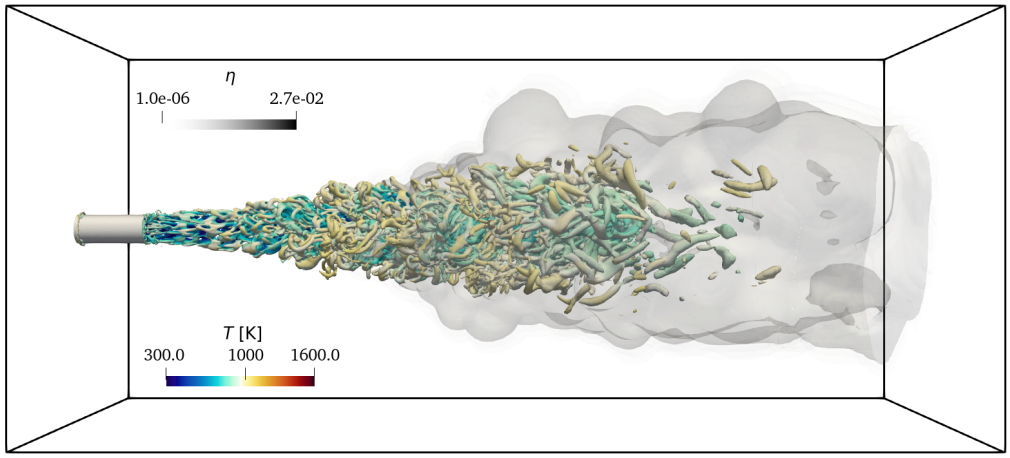

Figure 10: Instantaneous iso-surface of Q criterion, colored by temperature. Iso-contours of passive scalar denoting the prediction of auto-ignition.

In order to further analyze whether the auto-ignition distance is predicted correctly by η, two-dimensional cross-sections of the instantaneous flow field are depicted in Fig. 11. The comparison with the reactive case is shown next to it as (b). The temperature and the passive scalar are displayed at the top and bottom respectively. The white line contours are drawn the passive scalar satisfying auto-ignition. The structure of the ignition front takes a W-shape similar to the one obtained in the reactive simulations. The position of the peak is located around z/D =10, which gives excellent predictions of

auto-ignition.

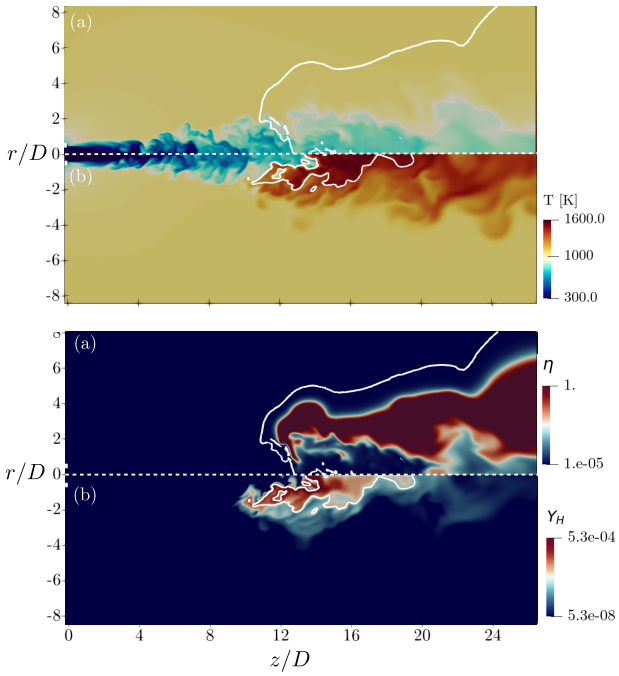

Figure 11: Two dimensional cross-section of instantaneous flow field. Temperature and η are presented with (a) compared with the reactive test case (b). Auto-ignition condition ($\eta = Y^0_{H_2}/10000$) is presented with white line contours for non reactive and $Y_{OH} = 600$ PPM as taken from Cabra et al. [10].

5.1. Mean quantities

The mean fields resulting from the previous simulations are presented through two-dimensional cross-sections in Fig. 12. In the same fashion as the instantaneous fields, the rapid increase of passive scalar reveals the position of auto-ignition. The averaged passive scalar contours show the same behavior as the instantaneous where the ignition point is met around z/D =10.

5.2. Further analyses : ignition and failure

The influence of the coflow temperature on the H_{lift} is further examined in Fig 13. The predictions from the passive scalar are compared to those

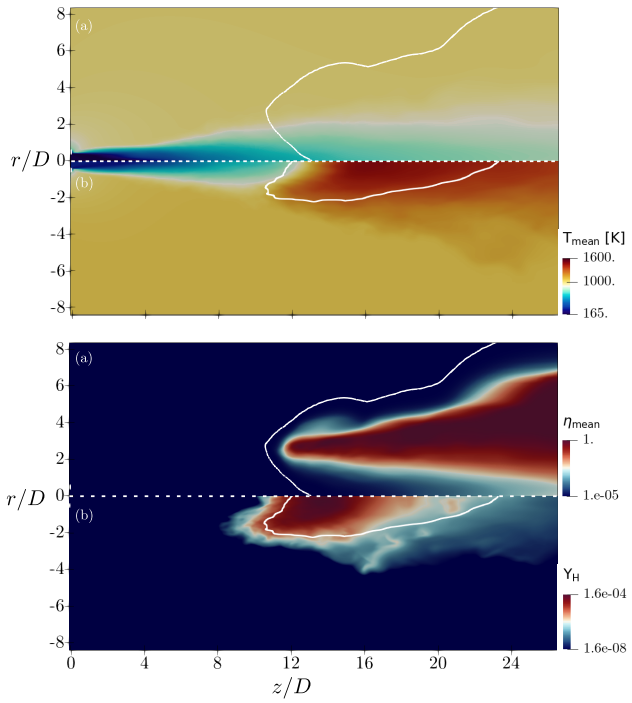

Figure 12: Two dimensional cross-section of averaged flow field. Top : Temperature T_{mean} and $Y_{\mathrm{H},mean}$ in the reactive case. Bottom : Temperature T_{mean} and passive scalar η_{mean} in the non reactive case.

from reactive simulations over a temperature range of 1025 to 1055 K. The lift-off height is sensitive (inversely Proportional) to the coflow temperature as can be found in experiments [20, 72]. Below 1030 K, the ignition occurs at a distance beyond the domain length. Hence, no ignition is observed. The results of the passive scalar prediction are consistent with the measurements obtained by the reactive simulations. This attests to the ability of the passive scalar to adapt to temperature variations. Beyond a coflow temperature of 1055 K, the flame flashes back to the inlet and no lift-off is observed.

To further understand the effectiveness of the model, it is important to analyze its behavior in predicting the absence of auto-ignition in a flow.

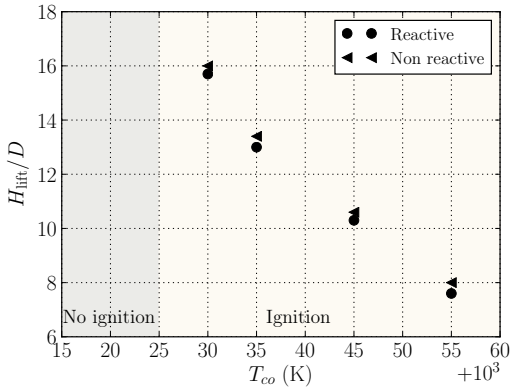

Figure 13: The effect of coflow temperature T_{co} on the lift-off height normalized by the jet diameter. Comparison between the reactive simulations and predictions form the passive scalar.

For this purpose, we performed a simulation at a relatively cold initial co-flow condition $T_0 = 1000$ K. The results obtained are shown in fields of Fig. 14. The upper field shows the evolution of the H radical from the reactive simulation. The initial temperature values are high enough to give reaction radicals but low enough to prevent a branching explosion. Thus, we observe traces at the interface of the central jet and the co-flow reaching maximum values of $Y_{\mathrm{H}} = 10^{-10}$. The passive scalar field is presented at the bottom. The maximum value reached by the passive scalar seems to be low enough to attest to the absence of ignition. Thus the passive scalar modeling seems to be efficient even in predicting non-igniting scenarios.

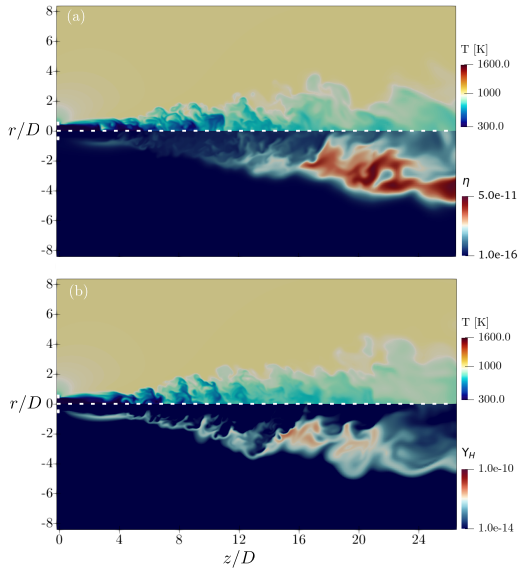

Figure 14: Two dimensional cross-section of instantaneous flow field of the jet. Comparison of radical pool production (Y_{H}) and passive scalar behavior for initial co-flow temperature 1000 K.

6. Conclusion

Numerical simulations of a 3D reactive jet in hot co-flow were conducted using Lattice Boltzmann Methods. Validation against experimental results of the average quantities (i.e temperature, species mass fractions) attested to the relevance of the Lattice Boltzmann Methods in turbulent combustion applications.

A novel passive scalar is derived from an eigenvalue analysis of the Jacobian of the chain branching chemistry in order to capture auto-ignition. Since ignition of hydrogen air is governed by the turbulent chemistry interaction. The proposed model is derived from the behavior of chemical reaction radicals and have the same chemical characteristics (i.e. it behaves as any mass fraction equation). However, the passive scalar has no interaction with

the flow. The latter does not modify the flow properties and takes only information from it. Thus, it is possible to apply most of the subgrid models developed in the literature for the different regimes of turbulent combustion. Results have shown that the model can capture accurately the experimental prediction of the auto-ignition in the jet flame. Moreover, the model is sensitive to co-flow temperature variation which felt in line with experimental observations. The absence of auto-ignition can also be predicted when the co-flow temperature is not enough to enhance chemical branching leading to ignition. Thus, this formulation can be helpful to predict ignition hazards in hydrogen leaks in complex configurations. In addition, its application to non-reactive simulations allows faster computations by removing the fast chemical hydrogen timescales.

Acknowledgements

Centre de Calcul Intensif d'Aix-Marseille and GENCI (Grant 2022 - A0112B11951) are acknowledged for granting access to their high performance computing resources. This research was supported by the MALBEC ANR project ANR-20-CE05-0009.

References

[1] A. L. Sánchez, F. A. Williams, Recent advances in understanding of flammability characteristics of hydrogen, Prog. Energ. Combust. 41 (2014) 1–55.

[2] B. Lewis, G. Von Elbe, Combustion, flames and explosions of gases, Academic Press, 1987.

[3] A. L. Sánchez, E. Fernández-Tarrazo, F. A. Williams, The chemistry involved in the third explosion limit of h2–o2 mixtures, Combust. Flame 161 (2014) 111–117.

[4] C. Treviño, Ignition phenomena in h_2-o_2 mixtures, in: W. A. Sirignano, J. Leyer, A. A. Borisov, A. L. Kuhl (Eds.), Dynamics of deflagrations and reactive systems–flames, AIAA, 1991, pp. 19–43.

[5] C. Treviño, A. Liñán, Numerical and asymptotic analysis of ignition processes, in: J. Buckmaster, T. L. Jackson, A. Kumar (Eds.), Combustion in High-Speed Flows, Springer, 1994, pp. 477–490. doi:10.1007/978-94-011-1050-1_17.
URL https://doi.org/10.1007/978-94-011-1050-1_17

[6] G. Del Alamo, F. Williams, A. Sanchez, Hydrogen-oxygen induction times above crossover temperatures, Combust. Sci. Technol. 176 (2004) 1599–1626.

[7] P. Boivin, A. L. Sánchez, F. A. Williams, Explicit analytic prediction for hydrogen–oxygen ignition times at temperatures below crossover, Combust. Flame 159 (2012) 748–752.

[8] X. Wang, C. K. Law, An analysis of the explosion limits of hydrogen-oxygen mixtures, J. Chem. Phys. 138 (2013) 134305. doi:10.1039/C7CP05639G.
URL http://dx.doi.org/10.1039/C7CP05639G

[9] P. Boivin, A. Sánchez, F. Williams, Analytical prediction of syngas induction times, Combust. Flame 176 (2017) 489–499.

[10] R. Cabra, T. Myhrvold, J. Y. Chen, R. W. Dibble, A. N. Karpetis, R. S. Barlow, Simultaneous laser raman-rayleigh-lif measurements and numerical modeling results of a lifted turbulent H2/N2 jet flame in a vitiated coflow, Proc. Combust. Inst. 29 (2002) 1881–1888.

[11] P. Domingo, L. Vervisch, D. Veynante, Large-eddy simulation of a lifted methane jet flame in a vitiated coflow, Combust. Flame 152 (2008) 415–432.

[12] R. L. Gordon, A. R. Masri, S. B. Pope, G. M. Goldin, Transport budgets in turbulent lifted flames of methane autoigniting in a vitiated co-flow, Combust. Flame 151 (2007) 495–511.

[13] R. R. Cao, S. B. Pope, A. R. Masri, Turbulent lifted flames in a vitiated coflow investigated using joint pdf calculations, Combust. Flame 142 (2005) 438–453.

[14] M. Ihme, Y. C. See, Prediction of autoignition in a lifted methane/air flame using an unsteady flamelet/progress variable model, Combust. Flame 157 (2010) 1850–1862.

[15] C. Duwig, L. Fuchs, Large eddy simulation of a h2/n2 lifted flame in a vitiated co-flow, Combust. Sci. Technol. 180 (2008) 453–480.

[16] C. Duwig, Large eddy simulation of flame stabilisation dynamics and vortex control in a lifted h2/n2 jet flame, Combust. Theor. Model. 15 (2011) 325–346.

[17] S. Kumar, P. Paul, H. Mukunda, Prediction of flame liftoff height of

diffusion/partially premixed jet flames and modeling of mild combustion burners, Combust. Sci. Technol. 179 (2007) 2219–2253.

[18] A. Masri, R. Cao, S. Pope, G. Goldin, Pdf calculations of turbulent lifted flames of h2/n2 fuel issuing into a vitiated co-flow, Combust. Theor. Model. 8 (2003) 1.

[19] C. Markides, E. Mastorakos, An experimental study of hydrogen autoignition in a turbulent co-flow of heated air, Proc. Combust. Inst. 30 (2005) 883–891.

[20] P. R. Medwell, B. B. Dally, Experimental observation of lifted flames in a heated and diluted coflow, Energ. Fuel 26 (2012) 5519–5527.

[21] A. Cavaliere, M. De Joannon, Mild combustion, Prog. Energ. Combust. 30 (2004) 329–366.

[22] G. Farag, S. Zhao, T. Coratger, P. Boivin, G. Chiavassa, P. Sagaut, A pressure-based regularized lattice-boltzmann method for the simulation of compressible flows, Phys. Fluids 32 (2020) 066106.

[23] M. Tayyab, S. Zhao, Y. Feng, P. Boivin, Hybrid regularized lattice-boltzmann modelling of premixed and non-premixed combustion processes, Combust. Flame 211 (2020) 173–184.

[24] G. Farag, T. Coratger, G. Wissocq, S. Zhao, P. Boivin, P. Sagaut, A unified hybrid lattice-boltzmann method for compressible flows: Bridging between pressure-based and density-based methods, Phys. Fluids 33 (2021) 086101.

[25] P. Boivin, M. Tayyab, S. Zhao, Benchmarking a lattice-boltzmann solver for reactive flows: Is the method worth the effort for combustion?, Phys. Fluids 33 (2021) 071703.

[26] T. Poinsot, D. Veynante, Theoretical and numerical combustion, RT Edwards, Inc., 2005.

[27] P. J. Linstrom, W. G. Mallard, The nist chemistry webbook: A chemical data resource on the internet, J Chem. Eng. Data 46 (2001) 1059–1063.

[28] A. Vreman, An eddy-viscosity subgrid-scale model for turbulent shear flow: Algebraic theory and applications, Phys. Fluids 16 (2004) 3670–3681.

[29] M. H. Silvis, R. A. Remmerswaal, R. Verstappen, Physical consistency of subgrid-scale models for large-eddy simulation of incompressible turbulent flows, Phys. Fluids 29 (2017) 015105.

[30] F. Trias, D. Folch, A. Gorobets, A. Oliva, Building proper invariants for eddy-viscosity subgrid-scale models, Phys. Fluids 27 (2015) 065103.

[31] P. Boivin, A. Dauptain, C. Jiménez, B. Cuenot, Simulation of a supersonic hydrogen–air autoignition-stabilized flame using reduced chemistry, Combust. Flame 159 (2012) 1779–1790.

[32] S. Chen, G. D. Doolen, Lattice boltzmann method for fluid flows, Annu. Rev. Fluid Mech. 30 (1998) 329–364.

[33] M. E. Gleason, B. Duncan, J. Walter, A. Guzman, Y.-C. Cho, Comparison of computational simulation of automotive spinning wheel flow field

with full width moving belt wind tunnel results, SAE Int. Passenger Cars Mech. Syst. 8 (2015) 275–293.

[34] G. Romani, D. Casalino, Rotorcraft blade-vortex interaction noise prediction using the lattice-boltzmann method, Aerosp. Sci. Technol. 88 (2019) 147–157.

[35] R. Löhner, Towards overcoming the les crisis, Int. J. Comput. Fluid. D. 33 (2019) 87–97.

[36] S. Succi, The lattice Boltzmann equation: for fluid dynamics and beyond, Oxford university press, 2001.

[37] P. Lallemand, L.-S. Luo, Theory of the lattice boltzmann method: Dispersion, dissipation, isotropy, galilean invariance, and stability, Phys. Rev. E 61 (2000) 6546.

[38] M. Geier, A. Greiner, J. G. Korvink, Cascaded digital lattice boltzmann automata for high reynolds flow, Phys. Rev. E 73 (2006) 066705.

[39] M. Geier, A. Greiner, J. G. Korvink, A factorized central moment lattice boltzmann method, Eur. Phys. J. Spec. Top. 171 (2009) 55–61.

[40] F. Dubois, T. Février, B. Graille, On the stability of a relative velocity lattice boltzmann scheme for compressible navier–stokes equations, C.R. Mec. 343 (2015) 599–610.

[41] A. De Rosis, K. H. Luo, Role of higher-order hermite polynomials in the central-moments-based lattice boltzmann framework, Phys. Rev. E 99 (2019) 013301.

[42] H. Chen, R. Zhang, I. Staroselsky, M. Jhon, Recovery of full rotational invariance in lattice boltzmann formulations for high knudsen flows, Physica A 362 (2006) 125–131.

[43] M. Geier, M. Schönherr, A. Pasquali, M. Krafczyk, The cumulant lattice boltzmann equation in three dimensions: Theory and validation, Comput. Math. Appl. 70 (2015) 507–547.

[44] M. Geier, A. Pasquali, M. Schönherr, Parametrization of the cumulant lattice boltzmann method for fourth order accurate diffusion part i: Derivation and validation, J. Comput. Phys. 348 (2017) 862–888.

[45] M. Geier, A. Pasquali, Fourth order galilean invariance for the lattice boltzmann method, Comput. Fluids 166 (2018) 139–151.

[46] J. Jacob, P. Sagaut, Wind comfort assessment by means of large eddy simulation with latice boltzmann method in full scale city area, Build. Environ. 139 (2018) 110–124.

[47] Y. Feng, M. Tayyab, P. Boivin, A lattice-boltzmann model for low-mach reactive flows, Combust. Flame 196 (2018) 249–254.

[48] G. Farag, S. Zhao, G. Chiavassa, P. Boivin, Consistency study of lattice-boltzmann schemes macroscopic limit, Phys. Fluids 33 (2021) 037101.

[49] Y. Feng, M. Tayyab, P. Boivin, A lattice-boltzmann model for low-mach reactive flows, Combust. Flame 196 (2018) 249 – 254.

[50] M. Tayyab, B. Radisson, C. Almarcha, B. Denet, P. Boivin, Experimen-

tal and numerical lattice-boltzmann investigation of the darrieus–landau instability, Combust. Flame 221 (2020) 103–109.

[51] K. Bhairapurada, B. Denet, P. Boivin, A lattice-boltzmann study of premixed flames thermo-acoustic instabilities, Combust. Flame 240 (2022) 112049.

[52] M. Tayyab, S. Zhao, P. Boivin, Lattice-boltzmann modeling of a turbulent bluff-body stabilized flame, Phys. Fluids 33 (2021) 031701.

[53] T. Krüger, H. Kusumaatmaja, A. Kuzmin, O. Shardt, G. Silva, E. M. Viggen, The lattice boltzmann method, Springer International Publishing 10 (2017) 978–3.

[54] J. Jacob, O. Malaspinas, P. Sagaut, A new hybrid recursive regularised bhatnagar–gross–krook collision model for lattice boltzmann method-based large eddy simulation, J. Turbul. 19 (2018) 1051–1076.

[55] M. Bauer, U. Rüde, An improved lattice boltzmann d3q19 method based on an alternative equilibrium discretization, arXiv preprint arXiv:1803.04937 (2018).

[56] M. Bauer, G. Silva, U. Rüde, Truncation errors of the d3q19 lattice model for the lattice boltzmann method, J. Comput. Phys. 405 (2020) 109111.

[57] S. Zhao, G. Farag, P. Boivin, P. Sagaut, Toward fully conservative hybrid lattice boltzmann methods for compressible flows, Phys. Fluids 32 (2020) 126118.

[58] F. Osmanlic, C. Körner, Lattice Boltzmann method for Oldroyd-B fluids, Comput. Fluids 124 (2016) 190–196.

[59] Y.-L. Feng, S.-L. Guo, W.-Q. Tao, P. Sagaut, Regularized thermal lattice boltzmann method for natural convection with large temperature differences, Int. J. Heat Mass Transfer 125 (2018) 1379–1391.

[60] Y. Feng, P. Sagaut, W. Tao, A three dimensional lattice model for thermal compressible flow on standard lattices, J. Comput. Phys. 303 (2015) 514–529.

[61] S. Marié, D. Ricot, P. Sagaut, Comparison between lattice boltzmann method and navier–stokes high order schemes for computational aeroacoustics, J. Comput. Phys. 228 (2009) 1056–1070.

[62] N. Smith, R. Bilger, C. Carter, R. Barlow, J.-Y. Chen, A comparison of cmc and pdf modelling predictions with experimental nitric oxide lif/raman measurements in a turbulent h2 jet flame, Combust. Sci. Technol. 105 (1995) 357–375.

[63] S. Pope, Computations of turbulent combustion: progress and challenges, in: Symp. (Int.) Combust., Vol. 23, Elsevier, 1991, pp. 591–612.

[64] J.-Y. Chen, W. Kollmann, Pdf modeling of chemical nonequilibrium effects in turbulent nonpremixed hydrocarbon flames, in: Symp. (Int.) Combust., Vol. 22, Elsevier, 1989, pp. 645–653.

[65] M. C. Melaaen, Analysis of curvilinear non-orthogonal coordinates for numerical calculation of fluid flow in complex geometries, Ph.D. thesis (1990).

[66] B. E. Launder, G. J. Reece, W. Rodi, Progress in the development of a reynolds-stress turbulence closure, J. Fluid Mech. 68 (1975) 537–566.

[67] I. R. Gran, B. F. Magnussen, A numerical study of a bluff-body stabilized diffusion flame. part 1. influence of turbulence modeling and boundary conditions, Combust. Sci. Technol. 119 (1996) 171–190.

[68] I. S. Ertesvåg, Turbulent flow and combustion, Tapir Academic Publisher, Trondheim (2000).

[69] X. Wang, V. Robin, A. Mura, A normalised residence time transport equation for the numerical simulation of combustion with high-temperature air, Combust. Theor. Model. 23 (2019) 821–853.

[70] W. Jones, S. Navarro-Martinez, Large eddy simulation of autoignition with a subgrid probability density function method, Combust. Flame 150 (2007) 170–187.

[71] P. Boivin, Reduced-kinetic mechanisms for hydrogen and syngas combustion including autoignition, Ph.D. thesis (2011).

[72] Y. Hu, R. Kurose, Large-eddy simulation of turbulent autoigniting hydrogen lifted jet flame with a multi-regime flamelet approach, Int. J. Hydrogen Energy 44 (2019) 6313–6324.